Resonance fluorescence from quantized one-dimensional molasses

P. Marte, R. Dum, R. Taïeb, and P. Zoller
Joint Institute for Laboratory Astrophysics, University of Colorado, Boulder, Colorado 80309-0440
(Received 13 August 1992)

We study theoretically the spectrum of resonance fluoresence from one-dimensional molasses consisting of two-level atoms with Zeeman substructure. The center-of-mass motion of the atom is treated fully quantum mechanically. The spectrum shows sidebands due to transitions between vibrational levels in optical potentials generated by the laser light. Detailed results are presented for the $J_g=\frac{1}{2}\rightarrow J_e=\frac{3}{2}$ atomic transition in a laser configuration with two counterpropagating waves with orthogonal polarizations. We have solved the corresponding quantum master equation and calculated the relevant autocorrelation function of the atomic dipole using (i) a direct numerical solution of the master equation, (ii) a wave-function simulation of the master equation and correlation function employing periodic time-dependent Bloch wave functions, and (iii) a semiclassical bipotential calculation for the spectrum including a simple quantum correction.

PACS number(s): 42.50.Ar, 32.80.−t

I. INTRODUCTION

Two recent experiments have reported observations of motion-induced sidebands in the weak-field absorption spectrum [1] and in the resonance fluorescence spectrum [2] from one-dimensional (1D) optical molasses in a configuration consisting of two counterpropagating laser beams with orthogonal polarizations (for related experiments see also [3–6]). These experiments have demonstrated for the first time we believe quantization of atomic motion in optical molasses. Furthermore, these spectra provide a direct means to determine the final temperatures obtained in laser polarization gradient cooling [7].

In the present paper we present a theoretical study of the spectrum of resonance fluorescence for 1D molasses consisting of two-level atoms with Zeeman substructure corresponding to $J_g\rightarrow J_e$ transitions, including a full quantum treatment of the atomic center-of-mass degrees of freedom. Here we will present results we have obtained for a $J_g=\frac{1}{2}$ to $J_e=\frac{3}{2}$ transition in a lin $\perp$ lin laser configuration (defined in Fig. 1) with adiabatic elimination of the excited states. We have solved the corresponding quantum master equation and calculated the relevant autocorrelation function of the atomic dipole. We have made a systematic comparison of solving our model equations by three different approaches: (i) a direct numerical solution of the master equation by discretizing on a momentum grid, and calculating the dipole correlation function with the help of the quantum regression theorem; (ii) a wave-function simulation of the master equation [8–11] and correlation function employing periodic time-dependent Bloch wave functions; and (iii) a semiclassical bipotential calculation for the spectrum including a simple quantum correction in the $\frac{1}{2}$ to $\frac{3}{2}$ case. We have performed similar calculations for higher order $J_g\rightarrow J_e$ transitions, without adiabatic elimination and with different laser polarization configurations, and these results will be presented elsewhere.

The paper is organized as follows. In Sec. II we give a qualitative discussion of the basic physical mechanism and present first results for the spectrum for a $J_g=\frac{1}{2}\rightarrow J_e=\frac{3}{2}$ atom. In Sec. III we give the master equation for general J_g to J_e transitions, while Secs. IV and V develop the corresponding wave-function simulation procedure used to solve the master equation and compute the spectrum. A brief outline of the semiclassical approach is given in Sec. VI; Sec. VII discusses our results. Technical details are summarized in the Appendixes.

II. QUALITATIVE CONSIDERATIONS

The physical picture underlying the spectrum of resonance fluorescence from 1D molasses is illustrated in Figs. 1 and 2 for a $J_g=\frac{1}{2}$ to $J_e=\frac{3}{2}$ transition. Figure 1 shows the atomic configuration for this model, as first discussed in the context of semiclassical laser cooling (polarization gradient cooling) by Dalibard and Cohen-Tannoudji [12], and more recently in a quantum version by Castin and Dalibard [13–15]. We consider two counterpropagating linearly polarized laser beams, so that the positive-frequency part of the electric field is given by $\mathbf{E}_{\rm cl}^{(+)}(z,t)=\mathcal{E}(e^{ikz}\mathbf{e}_x+e^{-ikz}\mathbf{e}_y)e^{-i\omega t}$. By the substitution

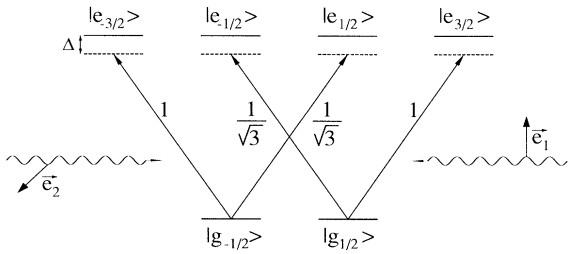

FIG. 1. Atomic-level scheme and Clebsch-Gordan coefficients for a $J_g=\frac{1}{2}$ to $J_e=\frac{3}{2}$ transition in a lin⊥lin configuration.

$z \rightarrow z - \lambda/8$ and a rotation by $\pi/4$ one gets the simpler form of an electric field with position-dependent polarization

$$\mathbf{E}_{\mathrm{cl}}^{(+)}(z,t) = \mathcal{E}[\sin(kz)\mathbf{e}_{+1} + \cos(kz)\mathbf{e}_{-1}]e^{-i\omega t}, \quad (1)$$

where ω is the frequency, $k = 2\pi/\lambda$ is the wave vector with λ the wavelength of the laser light, and $\mathbf{e}_{\pm 1}$ are spherical unit vectors.

For red laser detunings $\Delta = \omega - \omega_{eg}$ and low laser intensities, i.e., small saturation parameter $s = \Omega^2/2/(\Delta^2 + \Gamma^2/4) \ll 1$ with Ω the Rabi frequency and Γ the spontaneous decay width, the Stark shifts of the two $|g_-\rangle$ and $|g_+\rangle$ ground states will form an alternative pattern of optical bipotentials $U_\pm(z)$. This is shown in the upper part of Fig. 2: due to the large Clebsch-Gordan coefficients for the outer transitions (see Fig. 1), minima will occur for the state $|g_\pm\rangle$ at positions with pure $\sigma^\pm$ light. In addition, spontaneous emission causes transitions between these potentials via optical pumping processes.

In the semiclassical picture of Sisyphus cooling [12] one considers an atom moving on one of these potential curves, say $U_-(z)$. Transitions to the other potential $U_+(z)$ then occur preferentially from the tops of $U_-(z)$ down to the valleys of $U_+(z)$, so that on the average the atomic motion is damped. In Ref. [13] the center-of-mass motion of the atom is described fully quantum mechanically in terms of optical pumping transitions between the quantized energy levels (band structure) in the potentials $U_\pm(z)$. This picture is valid in the limit of level separations $\hbar\omega_{\mathrm{osc}}$ much larger than the optical pumping rate $\gamma_0 = 2/9s\Gamma$ (which implies large laser detunings). In the time domain this condition corresponds to a situation in which a wave packet in the potential undergoes many oscillations with frequency ω_{osc} before an optical pumping process occurs. The band structure is shown in the upper part of Fig. 2 for a potential with height $U_0 = 100E_R$ with $E_R = \hbar^2k^2/2M$ the recoil energy. U_0 is defined by $U_0 = -2/3s\Delta$. As a result of laser cooling the atom will occupy the lowest energy levels, and will thus be strongly localized: for the parameters of Fig. 2, we find that 32% of the population will be accumulated in the ground state and 20% in the first excited state [1]. The lower part of Fig. 2 shows the corresponding localization of the atom in minima of the $U_\pm(z)$ potentials. We have calculated these curves with the help of the wave-function simulation procedure described in detail in Secs. IV and V.

Sidebands in the spectrum of resonance fluorescence due to atomic motion can be interpreted as Raman transitions between the quantized energy bands. Figure 3 shows a typical spectrum. In this figure the spectrum $S_{\sigma=+1}(\nu)$ for σ^+ polarized photons of frequency ν is plotted for emission at a small angle with respect to the laser propagation axis z. The parameters are the same as in Fig. 2. The frequency ν is measured in units of the recoil energy relative to the laser frequency ω. This particular figure was obtained in an approximation where all the contributions from the various Raman transitions (Fig. 2) are added incoherently, i.e., neglecting interference between the lines (for details see Sec. VII and Appendix C). For the present parameters this provides a semiquantitative result for the spectrum—a comparison of this result with the full quantum calculations will be given in Sec. VII. The vertical lines in the lower part of this figure show the position of the transitions, as expected from the band structure (Fig. 2), and heights of these lines according to their integrated line strengths. The center peak in Fig. 3 consists of a coherent $\delta(\nu - \omega)$ function at the laser frequency and an incoherent background

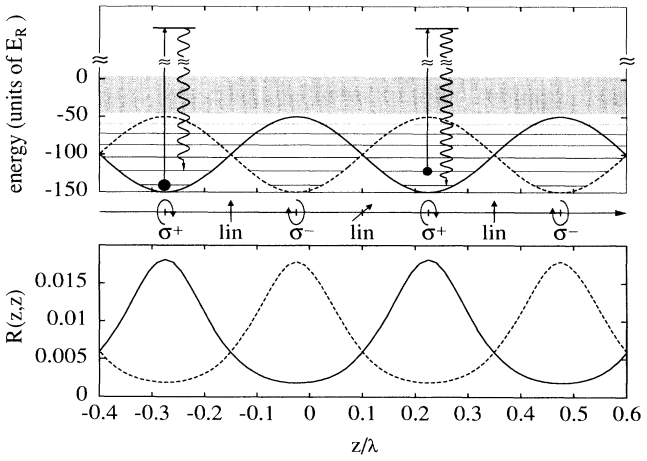

FIG. 2. In the upper panel the optical bipotentials and band structure of the atom are plotted as a function of position z for a $\frac{1}{2}$ to $\frac{3}{2}$ transition. The potential depth is $U_0 = 100E_R$. The excited states were adiabatically eliminated. We schematically indicate the two Raman processes between the ground and excited states which lead to the red and blue sidebands in resonance fluorescence. In the lower panel we show the spatial distribution of the atoms in the $|g_+\rangle$ state (solid line) and $|g_-\rangle$ state (dashed line) for $U_0 = 100E_R$ and $\gamma_0 = 5/3E_R$. The atoms are localized in the valleys of the corresponding optical potentials.

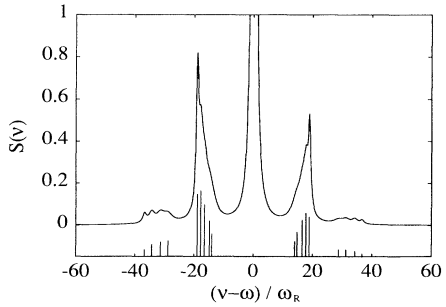

FIG. 3. Spectrum of resonance fluorescence $S_{+1}(\nu)$ for σ^+ polarized light as a function of the frequency ν for a $\frac{1}{2}, \frac{3}{2}$ transition. The parameters are $U_0 = 100E_R$ and $\gamma_0 = 5/3E_R$. The upper curves are results of adding up incoherently emission lines as discussed in the text. The vertical lines in the lower part of the figure show the positions and the expected heights of the emission lines for the two first sidebands, based on calculating Raman transition rates between the quantized energy levels. The excited states were adiabatically eliminated.

of finite width (see below). The red and blue first-order sidebands appear at frequencies corresponding to the transitions $E_n+\hbar\omega=E_{n+1}+\hbar\nu$ and $E_{n+1}+\hbar\omega=E_n+\hbar\nu$ with $n=0,1,\ldots$ principal quantum numbers for the energy bands [16]. Due to the anharmonicity of the potential these transition frequencies are different, so that each sideband consists of contributions from all of these closely spaced transitions. The intensity of each of these lines is related to the population of the initial states: an asymmetry of a stronger red sideband versus a weaker blue sideband indicates that there is more population in the ground state than in the first excited state, etc., and is thus a measure of the temperature of the molasses.

In Fig. 3 the first-order sidebands are dominated by the $0\leftrightarrow1$ peak, and have a shoulder due to the $1\leftrightarrow2$ transition which gives an asymmetric line shape: this is an indication that for the present parameters the substructure due to the various transitions $n\rightarrow n\pm1$ is almost resolved. The vertical lines in the lower part of Fig. 3 show the position of the emission lines and their expected height based on the interpretation in terms of Raman transitions between energy bands. The width of the incoherent central peak as well as widths of the individual lines in the sidebands are determined by the time scale of the redistribution rates $n\rightarrow n'$ $(n\neq n')$. For a constant spatial distribution of atoms we would expect this time scale to be of the order γ_0. In the present case, however, we see from Fig. 2 that the atoms are well localized in the potential wells compared with the scale given by the laser wavelength. Thus the Lamb-Dicke parameter $\eta=a/\lambda<1$ is small, where a is the localization length in one potential valley and λ the wavelength of the light. This situation is analogous to laser cooling of trapped ions in the Lamb-Dicke limit, and we refer to Ref. [17] for a discussion of resonance fluorescence from trapped ions. In the Lamb-Dicke limit the transition rates $n\rightarrow n'$ $(n\neq n')$ are suppressed [1] and are of the order $\eta^2\gamma_0$ for $\eta\ll1$. The widths of the individual lines in the spectrum will show this narrowing with increasing localization (for a more detailed discussion of this point we refer to Sec. VII and Fig. 7). For our parameter values a second much weaker sideband is also visible. Its substructure is better resolved than that of the first sideband.

We conclude this section with remarks about the different theoretical approaches presented in the following sections. From the above discussion we infer that in general a calculation of the spectrum of resonance fluorescence requires a theoretical model where the center-of-mass degrees of freedom are treated quantum mechanically. Furthermore, no adiabatic elimination of the internal degrees of freedom is possible, as the external motion ($\omega_{\rm osc}$) can be faster than the internal dynamics as given by the optical pumping rate between the Zeeman ground states (γ_0). In the following sections the quantum master equation (generalized optical Bloch equation) is solved by the following methods.

(i) Direct solution of the master equation. We have solved the master equation numerically by employing discretization in a momentum basis with a grid spacing given by the photon momentum $\hbar k$. This leads to a large number of ordinary coupled differential equations that can be integrated until the steady state is reached. The same method provides, via the quantum regression theorem, the dipole autocorrelation function and the spectrum. Alternatively, one can expand the density matrix in a basis of Bloch energy eigenfunctions of the optical potential. For $\omega_{\rm osc}\gg\gamma_0$ this gives, in a secular approximation, the population equations of Castin and Dalibard [13]. The same scheme can be employed to calculate the spectrum via the quantum regression theorem (for details see Appendix C). This leads to the physical picture of Raman transitions between the energy levels of the optical potential. The advantage of this approach is that it provides physical insight and in some cases semianalytical expressions for the spectrum in the limit of well-isolated sidebands.

(ii) Wave-function simulations [8–11]. For a system with a large number of degrees of freedom N, a direct solution of the master equation for the density matrix $\rho(t)$ becomes difficult due to its large dimension $N\times N$. In the present case N is the sum of the internal and (discretized) external degrees of freedom. As an alternative to solving the master equation for the density matrix one can *simulate* the time evolution of the system in terms of *N-component system wave functions* which undergo a sequence of quantum jumps (in the present case, optical pumping cycles). For large N—when solution of the density matrix becomes impractical—this quantum Monte Carlo approach can still provide a tractable means of obtaining spatial, momentum, and population distributions as well as spectra. This simulation is equivalent to an exact solution of the master equation, apart from the statistical error inherent in any simulation approach. In the present problem we simulate a spatially periodic density matrix by propagating *time-dependent Bloch functions* in the optical potential wells (see Fig. 2) while undergoing a sequence of optical pumping cycles (Sec V). This approach is of particular interest because it can be extended to two and three dimensions.

(iii) Semiclassical bipotential motion. Finally it is of interest to compare the spectra obtained by a fully quantum-mechanical approach with those obtained by a semiclassical method. The basic assumption of a semiclassical approximation is an expansion $\hbar k\ll\Delta p$, with Δp the width of the momentum distribution. For the parameter values studied in the present paper this assumption is reasonably valid. A second assumption is that there is no atomic coherence between the atomic ground state Zeeman levels: while this is true for the special case of a $\frac{1}{2}$ to $\frac{3}{2}$ transition (with the excited states adiabatically eliminated), the assumption of small Raman coherences between ground states is not *a priori* correct for higher angular momenta transitions. For the $\frac{1}{2}$ to $\frac{3}{2}$ transition this gives a classical stochastic model of bipotential motion [14,18], and we will compare the spectra obtained from this model with results from the full quantum model. We emphasize that in most semiclassical treatments further simplifications are made: a common assumption is that the internal atomic degrees of freedom can be adiabatically eliminated (which leads to a Fokker-Planck equation for the center-of-mass distribution), and a second one is the assumption of a constant velocity

[18–22]. Both of these simplifications are incorrect in the present problem.

III. MODEL

A. Generalized optical Bloch equations

We consider the one-dimensional situation of an atom moving along the z axis in the electric field given by Eq. (1). The internal atomic degrees of freedom are modeled by a two-level system $\{|J_g M_g\rangle, |J_e M_e\rangle\}$ with Zeeman substructure corresponding to a $J_g \rightarrow J_e$ transition. Denoting by $\mathbf{P}_g$ and $\mathbf{P}_e$ the projection operators on the ground and excited atomic states, respectively, we write the atomic dipole operator as

$$\mathbf{D}=\mathbf{P}_e\mathbf{D}\mathbf{P}_g+\mathbf{P}_g\mathbf{D}\mathbf{P}_e\equiv\mathbf{D}^{(-)}+\mathbf{D}^{(+)}. \tag{2}$$

In the rotating-wave approximation, the interaction Hamiltonian between the laser and the atom is (we set $\hbar=1$) $H_1(\hat{z},t)=-\mathbf{D}^{(+)}\cdot\mathbf{E}_{\rm cl}^{(-)}(\hat{z},t)+\text{H.c.}$ Expanding the electric-field amplitude in a spherical basis,

$$\mathbf{E}_{\rm cl}^{(+)}z)=\mathcal{E}\sum_{\sigma=0,\pm1}\epsilon_\sigma(z)\mathbf{e}_\sigma^{*}e^{-i\omega t}\quad\left[\sum_\sigma|\epsilon_\sigma(z)|^2=1\right] \tag{3}$$

(in our model $\mathcal{E}$ is position independent), we can write H_1 as

$$H_1(\hat{z},t)=-\frac{\Omega}{2}\mathcal{D}(\hat{z})e^{i\omega t}+\text{H.c.} \tag{4}$$

with

$$\begin{aligned}&\mathcal{D}(z)=\sum_{\sigma=0,\pm1}(-1)^\sigma A_\sigma\epsilon_{-\sigma}(z),\\&\Omega=2\mathcal{E}\langle e\|D\|g\rangle/\sqrt{2J_e+1},\\&A_\sigma=\sum_{M_e,M_g}|J_gM_g\rangle\langle J_gM_g;1\sigma|J_eM_e\rangle\langle J_eM_e|(\sigma=0,\pm1).\end{aligned} \tag{5}$$

Here $\mathcal{D}(z)$ is the dipole operator, Ω the Rabi frequency, and A_σ an atomic lowering operator with $\langle J_gM_g;1\sigma|J_eM_e\rangle$ a Clebsch-Gordan coefficient for dipole transition $|e\rangle\rightarrow|g\rangle$ with polarization $\sigma=0,\pm1$.

The generalized optical Bloch equations for an atom moving in the field (1) and coupled to a bath of vacuum modes of the radiation field are thus

$$\begin{aligned}\dot{\rho}=&-i(H_{\rm eff}\rho-\rho H_{\rm eff}^{\dagger})\\&+\Gamma\sum_{\sigma=0,\pm1}\int_{-k}^{+k}du\,N_\sigma(u)[e^{-iu\hat{z}}A_\sigma]\rho[A_\sigma^{\dagger}e^{+iu\hat{z}}]\end{aligned} \tag{6}$$

with

$$H_{\rm eff}=\frac{\hat{p}^2}{2M}+(-\Delta-i\tfrac{1}{2}\Gamma)\mathbf{P}_e+H_1(\hat{z})\equiv\frac{\hat{p}^2}{2M}+V(\hat{z}), \tag{7}$$

a non-Hermitian effective Hamiltonian. Equation (6) and $H_{\rm eff}$ are written in a rotating frame. $H_{\rm eff}$ describes the motion of the damped atom and its coupling to the laser driven internal atomic dynamics. The first term in $H_{\rm eff}$ (7) is the kinetic energy of the atom; $\Delta=\omega-\omega_{eg}$ denotes the laser detuning, and Γ is the spontaneous decay constant. The last term in (6) describes the recycling of the electron to the atomic ground state by spontaneous emission and the associated momentum transfer with angular distributions

$$\begin{aligned}N_0(u)&=\frac{3}{4k}\left[1-\left[\frac{u}{k}\right]^2\right],\\N_{\pm1}(u)&=\frac{3}{8k}\left[1+\left[\frac{u}{k}\right]^2\right].\end{aligned}$$

Remarks

(1) Adiabatic elimination of excited states. For low intensities, when the saturation parameter s is much less than 1, the excited states can be eliminated adiabatically. This gives the master equation for the density matrix of the ground-state manifold $\rho_{gg}=\mathbf{P}_g\rho\mathbf{P}_g$,

$$\begin{aligned}\dot{\rho}_{gg}=&-i(h_{\rm eff}\rho_{gg}-\rho_{gg}h_{\rm eff}^{\dagger})\\&+\gamma_0\sum_{\sigma=0,\pm1}\int_{-k}^{+k}du\,N_\sigma(u)[B_\sigma(\hat{z})e^{-iu\hat{z}}]\\&\times\rho_{gg}[e^{+iu\hat{z}}B_\sigma^{\dagger}(\hat{z})]\end{aligned} \tag{8}$$

where

$$h_{\rm eff}=\frac{\hat{p}^2}{2M}+\frac{s}{2}(\Delta-i\tfrac{1}{2}\Gamma)\mathcal{D}(\hat{z})\mathcal{D}^{\dagger}(\hat{z}) \tag{9}$$

and $B_\sigma(\hat{z})=A_\sigma\mathcal{D}^{\dagger}(\hat{z})$. The second term in (9) corresponds to the shift of the ground state and a width of the ground levels due to optical pumping. In a similar way, the operator $B_\sigma(\hat{z})e^{-iu\hat{z}}$ describes absorption of a laser photon followed by spontaneous emission with polarization σ including the momentum transfer to the atom. Explicit formulas for B_σ, etc. are given in Appendix A. We see that Eq. (8) is obtained from Eq. (6) by the substitutions

$$H_{\rm eff}\rightarrow h_{\rm eff},\quad\sqrt{\Gamma}A_\sigma\rightarrow\sqrt{\gamma_0}B_\sigma(\hat{z})\,. \tag{10}$$

(2) Symmetries and periodic stationary solutions. Translation by λ according to the operator $T_\lambda=e^{i\lambda\hat{p}}$ is a symmetry operation in our problem. Under the unitary transformation T_λ the master equation (6) remains form invariant: for ρ a solution of the master equation with Liouville $\mathcal{L}$, $T_\lambda\rho T_\lambda^{\dagger}$ will also be a solution of the *same* master equation (i.e., with the same $\mathcal{L}$). Actually, in view of $\mathbf{E}_{\rm cl}^{(+)}(z+\lambda/2,t)=-\mathbf{E}_{\rm cl}^{(+)}(z,t)$ the Bloch equation (6) is invariant under the transformation $T=T_{\lambda/2}(\mathbf{P}_e-\mathbf{P}_g)$ (see Refs. [23,18] for an analogous symmetry in the two-level system), and the adiabatically eliminated master equation (8) remains invariant under $T=T_{\lambda/2}$. Thus we define *periodic* stationary solutions R of the master equation according to $TRT^{\dagger}=R$. For the adiabatically eliminated problem this condition is

$$\langle z|R|z'\rangle=\langle z+\lambda/2|R|z'+\lambda/2\rangle \tag{11}$$

in the coordinate representation and

$$\langle p|R|p'\rangle\neq0\quad(\text{for } p-p'=0,\pm2\hbar k,\pm4\hbar k,\ldots) \tag{12}$$

in the momentum representation. Defining a Wigner function [18] $F(z,p)$ as a quasiprobability of position and momentum associated with R we see that this condition reads $F(z,p)=F(z+\lambda/2,p)$.

Note that the stationary periodic R is an improper solution as it cannot be normalized. On the other hand, integration of the generalized optical Bloch equations (6) and (8) for any normalized initial density operator $\rho(t=0)$ provides us with a solution $\rho(t)$ which is normalized at all times, $\mathrm{Tr}\rho(t)=1$. However, this normalized density operator $\rho(t)$ never reaches a steady-state spatial distribution. For long times, it is reasonable in our calculations to replace $\rho(t)$ by the periodic stationary R defined above, which is normalized on the unit cell. In particular, we approximate a normalized Wigner function $f(z,p,t)$ associated with $\rho(t)$ and with spatial extent $L=N\lambda$ (N is the number of unit cells) near the center of the distribution by $f(z,p,t)\simeq(1/N)F(z,p)$.

B. Spectrum of resonance fluorescence

The positive-frequency part of the electric field $\hat{\mathbf{E}}^{(+)}(\mathbf{x},t)$ in the Heisenberg picture has the mode expansion

$$\hat{\mathbf{E}}^{(+)}(\mathbf{x},t)=i\sum_{\sigma'}\int d^3k'\left[\frac{\hbar\omega_{k'}}{2\epsilon_0(2\pi)^3}\right]^{1/2}\times\epsilon_{\mathbf{k}'\sigma'}e^{i\mathbf{k}'\cdot\mathbf{x}}b_{\mathbf{k}'\sigma'}(t) \tag{13}$$

with $b_{\mathbf{k}'\sigma'}$ destruction operators for photons in the mode $(\mathbf{k}',\sigma')$. The Hamiltonian for the atom-vacuum field interaction is

$$H_{\mathrm{AF}}=-\int d^3x'\delta(\mathbf{x}-\hat{\mathbf{x}}(t))[\mathbf{D}^{(+)}\cdot\mathbf{E}^{(-)}(\mathbf{x}',t)+\mathrm{H.c.}], \tag{14}$$

which leads to the Heisenberg equation

$$\frac{d}{dt}b_{\mathbf{k}'\sigma'}(t)=-i\omega_{k'}b_{\mathbf{k}'\sigma'}(t)+\int d^3x'\left[\frac{\hbar\omega_{k'}}{2\epsilon_0(2\pi)^3}\right]^{1/2}e^{-i\mathbf{k}'\cdot\mathbf{x}'}\times\epsilon^*_{\mathbf{k}'\sigma'}\cdot\mathbf{D}^{(+)}\delta(x'-x(t)). \tag{15}$$

A simple definition of the spectrum is based on calculating the change in time of the occupation number of photons in the mode $(\mathbf{k}',\sigma')$,

$$S_{\mathbf{k}'\sigma'}=\frac{d}{dt}\langle b^\dagger_{\mathbf{k}'\sigma'}(t)b_{\mathbf{k}'\sigma'}(t)\rangle$$
$$=\frac{\omega'_k}{2\epsilon_0(2\pi)^3}\frac{\langle e\|d\|g\rangle^2}{2J_e+1}\int_0^t dt'e^{-i\omega_{k'}(t-t')}\langle A^\dagger_\sigma(t)e^{i\mathbf{k}'\cdot\hat{\mathbf{x}}(t)}A_{\sigma'}(t')e^{-i\mathbf{k}'\cdot\hat{\mathbf{x}}(t')}\rangle+\mathrm{c.c.}\quad(t\to\infty), \tag{16}$$

where the dipole correlation function follows from the quantum regression theorem

$$c_\sigma(t-t')=\langle A^\dagger_{\sigma'}(t)e^{i\mathbf{k}'\cdot\hat{\mathbf{x}}(t)}A_{\sigma'}(t')e^{-i\mathbf{k}'\cdot\hat{\mathbf{x}}(t')}\rangle$$
$$=\mathrm{Tr}\{A^\dagger_{\sigma'}e^{i\mathbf{k}'\cdot\hat{\mathbf{x}}}e^{\mathcal{L}(t-t')}A_{\sigma'}e^{-i\mathbf{k}'\cdot\hat{\mathbf{x}}}\rho(t')\}\qquad(t\geq t') \tag{17}$$

with $\mathcal{L}$ the master-equation operator. For large time differences we expect the correlation function to factorize; this gives rise to a coherent δ-function contribution in the spectrum. We simplify the spectrum (16) under the following assumptions: (i) To obtain a one-dimensional model we replace $\mathbf{k}'\cdot\hat{\mathbf{x}}$ by its projection on the z axis. (ii) We are interested in emission at small angles to the axis given by the laser propagation $\mathbf{k}$ (thus the polarization components of interest are $\sigma^\pm$), and we confine ourselves to frequencies which allow us to approximate $k'\hat{z}\approx k\hat{z}$ in the exponentials of Eq. (16). This is valid for $|k'-k|L\ll 1$ with L the dimension of the medium (the delocalized atom). (iii) In calculating the spectrum we use the improper stationary density matrix R which is periodic in λ. (iv) With adiabatic elimination of the excited states the expression for the spectrum is obtained by the substitution (10). A similar discussion for the spectrum can be given in terms of the autocorrelation function of the electic field in the far-field region.

IV. WAVE-FUNCTION SIMULATION FOR ρ

The Hilbert space underlying the dynamics of the generalized optical Bloch equations is the product space of center-of-mass wave packets $L^2(\mathbb{R})$, and the internal atomic degrees of freedom with dimension $(2J_g+1)+(2J_e+1)$ [or $(2J_g+1)$ in the adiabatically eliminated case]. Direct numerical solution of the master equation is complicated by the high dimensionality of the problem [the dimension of the density operator $\rho(t)$ is $N\times N$ for an N-dimensional system space]. As an alternative to solving the master equation, one can simulate the time evolution of the system in terms of system wave functions $|\phi,t\rangle$ (with dimension N). Apart from the finite sampling implicit in any simulation approach, no further approximations such as adiabatic elimination of the internal degrees of freedom or semiclassical approximations are made. Below we give an outline of the general wave-function simulation procedure for the master equations (6) and (8) and the dipole correlation function (16).

A. Generalized optical Bloch equations

Following our previous work [8] (see also Refs. [9–11]) a simulation approximation to the density matrix $\rho(t)$ is obtained as follows.

(i) Initial conditions. The initial state $\rho(t=0)$ can be specified as a pure state or a statistical mixture. Typical-

ly, $\rho(t=0)$ will be a product of a center-of-mass distribution and a density operator for atoms in the ground states [$\rho(t=0)=\rho_{\text{c.m.}}\otimes\rho_A$]. In this case, we choose a set of (normalized) initial wave functions $|\phi,t=0\rangle$ as a product of center-of-mass wave packets and atomic ground-state wave functions to represent this ensemble.

(ii) Propagation and quantum jumps. We propagate the system wave function $|\phi,t\rangle$ according to the Schrödinger equation

$$i\frac{d}{dt}|\phi,t\rangle=H_{\text{eff}}|\phi,t\rangle, \tag{18}$$

with H_{eff} the non-Hermitian Hamiltonian (7). This equation is a multicomponent Schrödinger equation, which determines the evolution of the system between two spontaneous emission events: Eq. (18) describes the coupled time evolution of the atomic center-of-mass wave packets and internal atomic structure, and the non-Hermitian part of H_{eff} corresponds to radiative damping due to emission of photons from the excited state. In particular, the probability density for spontaneous emission of a photon at time t in the direction u and with polarization σ is

$$\bar{c}(t,u,\sigma)=N_\sigma(u)\Gamma\| A_\sigma|\phi,t\rangle\|^2. \tag{19}$$

The time t, u, and σ of the "next quantum jump" can be simulated from (19). The wave function after the jump is

$$|\phi,t^+\rangle=A_\sigma e^{-iu\hat{z}}|\phi,t^-\rangle/\| A_\sigma e^{-iu\hat{z}}|\phi,t^-\rangle\|, \tag{20}$$

with t^+ (t^-) the time after (before) the jump. Thus spontaneous emission of a photon is associated with a transition from the excited state to the ground state (A_σ) and as kick of the center-of-mass of the atom ($e^{-iu\hat{z}}$) where the component u (the photon momentum along z) is drawn according to the distribution $N_\sigma(u)$. After the quantum jump we continue integration of (18) up to the next spontaneous emission, etc.

(iii) Simulation results. The density matrix is obtained from

$$\rho(t)=\langle\langle\,|\phi,t\rangle\langle\phi,t|/\||\phi,t\rangle\|^2\rangle\rangle, \tag{21}$$

where $\langle\langle\ \rangle\rangle$ denotes averaging over wave-function realizations. In the case where the excited states are eliminated, we make the replacement (10) in Eqs. (18) and (20), respectively.

B. Spectrum of resonance fluorescence

The spectrum of resonance fluorescence is proportional to the Fourier transform of the stationary dipole autocorrelation function (16). To derive a simulation procedure for the spectrum we consider the functional

$$S_t[f(t)]=\int_0^d dt' f(t')\langle e^{ik\hat{z}(t)}A_\sigma^\dagger(t)e^{-ik\hat{z}(t')}A_\sigma(t')\rangle, \tag{22}$$

with $f(t)$ a function to be specified below. Using the quantum regression theorem we rewrite (22)

$$S_t[f(t)]=\text{Tr}[e^{ik\hat{z}}A_\sigma^\dagger\rho_1(t)] \tag{23}$$

with

$$\rho_1(t)=\int_0^t dt' f(t')e^{\mathcal{L}(t-t')}e^{ik\hat{z}}A_\sigma\rho(t'). \tag{24}$$

Here $\mathcal{L}$ is the master operator and $\rho(t)$ the density operator according to (6). $\rho(t)$ and $\rho_1(t)$ obey the equations

$$\begin{aligned}\dot{\rho}(t)&=\mathcal{L}\rho(t),\\ \dot{\rho}_1(t)&=\mathcal{L}\rho_1(t)+f(t)e^{-ik\hat{z}}A_\sigma\rho(t).\end{aligned} \tag{25}$$

Following arguments given in Refs. [8–11], $\rho_1(t)$ (and thus $S_t[f(t)]$) can be simulated by propagating the pair of system wave functions

$$\begin{aligned}i\frac{d}{dt}|\phi,t\rangle&=H_{\text{eff}}|\phi,t\rangle,\\ i\frac{d}{dt}|B,t\rangle&=H_{\text{eff}}|B,t\rangle+if(t)e^{-ik\hat{z}}A_\sigma|\phi,t\rangle,\end{aligned} \tag{26}$$

where $|\phi,t\rangle$ is the system wave function introduced in Sec. IV A, and $|B,t\rangle$ can be interpreted as describing the weak perturbation of the system according to the source term involving the function $f(t)$. Equations (26) can be simulated with quantum jumps dictated by $|\phi,t\rangle$ [compare the discussion of Eq. (19)]. The jump condition for $|\phi,t\rangle$ is again given by Eq. (20), and the corresponding equation for $|B,t\rangle$ is

$$|B,t^+\rangle=e^{-iu\hat{z}}A_\sigma|B,t^-\rangle\|e^{-iu\hat{z}}A_\sigma|\phi,t^-\rangle\|. \tag{27}$$

Ensemble averaging gives

$$\rho_1(t)=\langle\langle\,|B,t\rangle\langle\phi,t|/\||\phi,t\rangle\|^2\rangle\rangle. \tag{28}$$

Note that both (27) and (28) involve normalization with respect to $|\phi,t\rangle$.

Two special cases for the function $f(t)$ are of interest.

(i) $f_\nu(t)=e^{+i\nu t}$: This gives the spectrum directly according to Eqs. (16)

$$S(\nu)=e^{-i\nu t}S_t[e^{i\nu t}]+\text{c.c.}\quad(t\to\infty). \tag{29}$$

This method requires that a perturbed wave function $|B_\nu,t\rangle$ is solved for *each* frequency component ν.

(ii) $f_{t_0}(t)=\delta(t-t_0)$: This gives the correlation function

$$\langle e^{ik\hat{z}(t)}A_\sigma^\dagger(t)e^{-ik\hat{z}(t_0)}A_\sigma(t_0)\rangle=\langle\langle\,\langle B_{t_0},t|e^{ik\hat{z}}A_\sigma^\dagger|\phi,t\rangle\rangle\rangle, \tag{30}$$

where $|B_{t_0},t\rangle$ for $t>t_0$ obeys the same *homogeneous* equation as $|\phi,t\rangle$ with initial condition at t_0 as imposed by the δ kick, $|B_{t_0},t_0^+\rangle=e^{-ik\hat{z}}A_\sigma|\phi,t_0\rangle$. To obtain the *stationary* correlation function as a function of $\tau=t-t_0$ these simulations have to be repeated for randomly distributed t_0. In the numerical calculations of this paper the second method was used.

From a physical point of view the first case corresponds to probing the system with a fixed frequency field, whereas in the second case the correlation function is derived by kicking the system with δ-function pulses.

V. WAVE-FUNCTION SIMULATION OF THE PERIODIC STATIONARY DENSITY MATRIX R

In Sec. III A we have argued that for sufficiently long times the density matrix $\rho(t)$ is well approximated by the periodic stationary solution R. Here we discuss the wave-function solution for R, and simulation of the corresponding spectrum of resonance fluorescence.

In view of the translational invariance of $H_{\rm eff}$, A_σ and $B_\sigma(\hat{z})$ with respect to translations by λ we take for the Monte Carlo wave function the ansatz

$$\langle z|\phi_q,t\rangle=\frac{1}{\sqrt{2\pi}}e^{iqz}u_q(z,t), \tag{31}$$

with $u_q(z,t)=u_q(z+\lambda,t)$ the periodic part of the time-dependent Bloch function and $q\in(-k/2,k/2]$ a quasimomentum in the first Brillouin zone. The Schrödinger equation for $u_q(z,t)$ is

$$i\frac{\partial}{\partial t}u_q(z,t)=H_{\rm eff}^{(q)}u_q(z,t)\equiv\left[\frac{(\hat{p}+q)^2}{2M}+V(z)\right]u_q(z,t) \quad (0\le z\le\lambda). \tag{32}$$

Note that the quasimomentum q now appears as a shift of the momentum in the kinetic-energy term. The wave function (31) describes a periodic system with finite extent and $\langle z|\phi_q,t\rangle$ is an improper wave function. We choose to normalize the wave function on the unit cell, restricting us to the Hilbert space $L^2([0,\lambda))$. Propagation of the Bloch function according to (32) can be done very efficiently employing a fast Fourier transform (FFT) split operator method [24] outlined in Appendix B.

Consider now the action of the jump operator $B_\sigma(\hat{z})$ on the Bloch wave function (31). We have

$$e^{-iuz}B_\sigma(z)[e^{iqz}u_i(z,t^-)]=e^{i(q-u)z}[B_\sigma(z)u_q(z,t^+)] \propto e^{iq'z}u_{q'}(z,t^+), \tag{33}$$

where $q'=q-u+nk\in(-k/2,k/2]$ with $n=0,\pm1$ the quasimomentum after emission, i.e., the initial quasimomentum q minus the momentum transfer due to the photon shifted by $0,\pm k$ back to the first Brillouin zone. Thus a quantum jump of the Bloch wave function with quasimomentum q produces another Bloch state with quasimomentum q' given by Eq. (33) and

$$u_{q'}(z,t)\propto B_\sigma(z)e^{-i(u+nk)z}u_q(z,t). \tag{34}$$

The quasimomentum q, therefore, plays the role of a "family index": q is preserved during the propagation (32) between two spontaneous emissions, while spontaneous emission mixes the different families $q\to q'$. It is straightforward to generalize these equations to the calculation of the spectrum and dipole correlation function (see Sec. IV B).

Thus a wave-function simulation of the stationary periodic density matrix proceeds as follows. First we propagate a Bloch function (31), with arbitrarily chosen initial $\langle z|\phi_q,t=0\rangle$, according to (32) and (33) over a time interval large compared with the cooling time, i.e., over a time during which the periodic ensemble reaches the stationary state. In the steady state we follow a *single* Monte Carlo wave function, replacing ensemble averages by time averages, and taking "measurements" of the spatial, momentum, and energy distributions, etc. (see remarks below) at time steps large enough to guarantee statistical independence. This gives us the periodic density matrix

$$\langle z|R|z'\rangle=\langle\langle[e^{iqz}u_q(z,t)][e^{iqz'}u_q(z',t)]^\dagger\rangle\rangle\ . \tag{35}$$

Remarks

(1) For the stationary periodic density matrix (35) there are no coherences between different families $q\neq q'$ [compare Eq. (11)]. We emphasize that in the wave-function simulation the quasimomentum q is treated as a continuous variable (and is not discretized as in our numerical solution of the master equation).

(2) Consider a single "measurement of the spatial and/or momentum distribution" for a given Bloch function (31) at time t in the Monte Carlo simulation. The (periodic) spatial distribution of atoms in the atomic state i is

$$P_i(z,t)=|\langle z,i|\phi_q,t\rangle|^2\equiv|u_{qi}(z,t)|^2. \tag{36}$$

The momentum distribution is

$$P_i(p,t)=|\langle p,i|\phi_q,t\rangle|^2=\sum_{m=-\infty}^{+\infty}\delta(p-q-mk)|c_{qi}^{(m)}(t)|^2 \tag{37}$$

with a Fourier expansion for the Bloch functions

$$u_{qi}(z,t)=\sum_{m=-\infty}^{+\infty}c_{qi}^{(m)}(t)e^{imkz}, \tag{38}$$

where the coefficients $c_{qi}^{(m)}(t)$ are provided directly by the FFT algorithm of Appendix B. A similar expression can be derived for the Wigner function.

(3) In the limit where the laser-induced conservative potentials in $H_{\rm eff}$ (7) and (9) are much larger than the imaginary part (i.e., the widths introduced by radiative decay or optical pumping), the results for the spectrum of resonance fluorescence can be readily interpreted in terms of transitions between band-structure eigenstates of a Hamiltonian $H=\hat{p}^2/2M+U(z)$ obtained from $H_{\rm eff}$ by setting the non-Hermitian part equal to zero. With the Bloch ansatz $\langle z|\alpha q\rangle=1/\sqrt{2\pi}e^{iqz}u_{q\alpha}(z)$ we have the eigenvalue problem

$$H^{(q)}u_{\alpha q}(z)\equiv\left[\frac{(\hat{p}+q)^2}{2M}+U(z)\right]u_{q\alpha}(z)=E_{\alpha q}u_{\alpha q}(z) \tag{39}$$

with α a set of quantum numbers labeling the bands. This band structure is illustrated for the $J_g=\frac{1}{2}\to J_e=\frac{3}{2}$ together with potentials in Fig. 2.

Wave packets of Bloch states are superpositions

$$\langle z|\phi,t\rangle=\sum_\alpha\int_{-k}^{+k}dq\ a_{\alpha q}(t)e^{[iqz}u_{\alpha q}(z), \tag{40}$$

while the Bloch wave functions (31) used in the simulations are superpositions of states with different α but fixed q,

$$\langle z|\phi_q,t\rangle = e^{iqz}u_q(z,t) \equiv \sum_\alpha a_{\alpha q}(t)e^{iqz}u_{\alpha q}(z). \tag{41}$$

Equation (41) is a wave packet periodically repeated with λ. As we remarked before, the density matrix (35) has no coherences $q \neq q'$, but will in general develop atomic coherences between different α quantum numbers.

Energy distributions of the Bloch functions (31) with respect to the Hamiltonian H, which defines the energy bands, are

$$P(E,t)=\langle \phi_q,t|\delta(E-H)|\phi_q,t\rangle \equiv \langle u_q,t|\delta(E-H^{(q)})|u_q,t\rangle. \tag{42}$$

In practice, we introduce an energy window of width ΔE according to

$$P_{\Delta E}(E,t)=\left\langle u_q,t\left|\frac{\Delta E^{2K}}{(E-H^{(q)})^{2K}+\Delta E^{2K}}\right|u_q,t\right\rangle. \tag{43}$$

The parameter K should be taken sufficiently large to obtain a rectangular window function; typically a value of $K=2$ is sufficient. As outlined in detail in Ref. [25], Eq. (43) can be calculated by solving a set of K inhomogeneous Schrödinger equations. We have used this scheme as one way to find the populations of the energy bands.

VI. SEMICLASSICAL SPECTRA

As mentioned in Sec. II, for the $J_g=\frac{1}{2}$ to $J_e=\frac{3}{2}$ transitions the ground-state coherences are exactly zero after adiabatic elimination. This allows a classical interpretation of the time evolution of the atom in terms of motion in a bipotential [14,22]. By taking the Wigner transform of Eq. (8) and subsequent expansion of $f(z,p+\hbar k,t)$ in $\hbar k$, we get

$$\left[\frac{\partial}{\partial t}+\frac{p}{m}\frac{\partial}{\partial z}-\frac{dU_\pm(z)}{dz}\frac{\partial}{\partial p}-D_\pm(z)\frac{\partial^2}{\partial p^2}\right]f_\pm(z,p,t) = \pm[\gamma_-(z)f_-(z,p,t)-\gamma_+(z)f_+(z,p,t)] + D_{\pm\mp}(z)\frac{\partial^2}{\partial p^2}f_\mp(z,p,t) \tag{44}$$

where

$$U_+(z)=U_0\cos^2(kz),\quad U_-(z)=U_0\sin^2(kz),$$
$$\gamma_+(z)=\gamma_0\cos(kz),\quad \gamma_-(z)=\gamma_0\sin^2(kz),$$
$$D_\pm(z)=\frac{\hbar k^2\Gamma s}{90}[35\pm 7\cos(2kz)],$$
$$D_{\pm\mp}(z)=\frac{\hbar k^2\Gamma s}{90}[6\mp\cos(2kz)], \tag{45}$$

with $f_\pm(z,p,t)$ the Wigner distribution of the population for the $|g_\pm\rangle$ states. The interpretation of the above equation is straightforward [26,27]. The left-hand side of Eq. (44) corresponds to Brownian motion in a potential $U_\pm(z)$, the diffusion $D_\pm$ being due to random kicks from the spontaneous emission of $\sigma^\pm$ photons. The right-hand side describes jumps between the potentials due to emission of π-polarized photons.

It is straightforward to solve (44) by simulation in a way analogous to the quantum version described in Sec. V. The simulation algorithm follows by expanding Eq. (44) for small time steps [26]: we start with an arbitrary initial condition z, p, and, e.g., state $|g_+\rangle$. We evolve $z(t)$ and $p(t)$ over a small time step Δt according to

$$dz(t)=p(t),dt,$$
$$dp(t)=-dU_+/dz\,dt+\sqrt{2D_+[z(t)]}\,dW(t), \tag{46}$$

where $W(t)$ is a Wiener process. The rate $\gamma_+(z)$ determines the probability of a jump from U_+ to U_-: if we find $[1-\gamma_0(z)\Delta t]<\eta$, where η is uniformly distributed random number in (0,1], we change the potential $+\rightarrow-$, and give the momentum $p(t)$ a random kick: $p\rightarrow p+\sqrt{2D_{+-}(z)/\gamma_+(z)}\,G$, where G is a random number with Gaussian distribution, etc. Finally, the momentum and space distributions are determined as histograms of realizations of $z(t)$ and $p(t)$ trajectories.

The asymmetry of sidebands in the spectrum of resonance fluorescence is a quantum feature. Semiclassical spectra are symmetric. To obtain the asymmetry in the spectrum we keep the momentum kicks due to photons in the semiclassical calculation of the two-time correlation function. Using the quantum regression theorem the two-time correlation $c_{+1}(t-t')$ may be written as $\mathrm{Tr}\{B^\dagger_{+1}(t)e^{+ik\hat{z}(t)}\rho_1(t)\}$ with

$$\rho_1(t)=e^{\mathcal{L}(t-t')}B_{+1}(t')e^{-ik\hat{z}(t')}\rho(t). \tag{47}$$

The Wigner transform reads

$$f_{1_+}=\frac{-i}{2\sqrt{2}}e^{L(t-t')}[3f_+(z,p,t) - e^{-2ikz}f_+(z,p-k,t')] \tag{48}$$

[where L is the master equation of Eq. (44) and a similar equation follows for f_{1_-}]. Note that the two terms on the right-hand side of the above equation correspond to two processes: the first term describes absorption of a laser photon and emission of a fluorescence photon in the same direction (with no net momentum transfer to the atom), and absorption and emission into opposite directions (with momentum transfer $2\hbar k$). We get

$$c_{+1}(t-t')=\sum_{j',j=\pm}\int dz\int dp\int dz'\int dp'[(1-e^{2ikz})\xi_{jj'}P(j,z,p,t|j',z',p',t') +(1-e^{2ikz})e^{-2ikz'}\xi_{jj'}P(j,z,p,t|j',z',p'-\hbar k,t)]f_{j'}(z',p'), \quad (49)$$

where we define the conditional probability density

$$P(j,z,p,t)|j',z',p',t')=[e^{L(t-t')}]_{jj'}\delta(z-z')\delta(p-p') \quad (50)$$

for the atom to be found at time t in state j at z,p, given it started in state j' at z',p' at time t'. The $\xi_{jj'}$ are weight factors due to the different transition rates: $\xi_{\pm\mp}=\frac{1}{3}$, $\xi_{++}=\frac{1}{9}$, and $\xi_{--}=1$.

VII. DISCUSSION

A first survey of the features of the spectrum and the numerical results for the configuration of Fig. 1 has already been given in Sec. II. In Fig. 2 we have plotted the band structure in the optical potential for $U_0=100E_R$, and have semiclassically indicated the Raman processes between the energy bands in the optical potential. Figure 3 is a resonance fluorescence spectrum obtained by adding incoherently the contributions from the various Raman lines: for a discussion of the spectrum in a basis of energy bands, see Appendix C. The vertical lines in the lower part of Fig. 3 at frequencies predicted by the band-structure calculation have heights proportional to the populations of the initial states times the square of the Raman transition matrix elements, $\langle q'n'g_{m'}|e^{-ik'\hat{z}B_\sigma(\hat{z})}|qn\,g_m\rangle$. Here $|qn\,g_m\rangle$ are Bloch energy eigenfunctions with q the quasimomentum, n the principal quantum number, and g_m the atomic-state label.

As outlined above, we have calculated the spectra $S_{\sigma=\pm1}(\nu)$ by three methods, a direct numerical solution of the quantum master equation, a wave function simulation, and a semiclassical approach. We find that the predictions of all three methods agree to within a few percent. As part of the calculations for the spectrum we obtained spatial and momentum distribution functions and populations of the vibrational levels in the optical potentials for polarization gradient cooling, in agreement with those given in Refs. [13,15]. In Figs. 4(a)–4(d) we compare the $\frac{1}{2}$-$\frac{3}{2}$ spectrum according to the three approaches for the same parameters as in Figs. 2 and 3: we plot the spectra calculated by (a) numerical solution of the master equation, (b) wave function simulation with 4000 realizations for the dipole correlation function, (c) wave function simulation with 80 000 realizations, and (d) the semiclassical spectrum (according to Sec. VI). Agreement between these calculations for both the position of the lines and the line shape is excellent, apart from some minor differences in details of the sharp features of the red sideband. For the present parameters we find almost quantitative agreement with the simple spectrum of Fig. 3 obtained by incoherently adding Raman transition lines. In addition, our approach allows us to compute the coherences $n-n'$ between the energy bands (which are neglected in the secular approximation [13,15]): for the parameter values of Fig. 4 these density-matrix coherences are two orders of magnitude smaller than the corresponding population terms. For the solution of the master equation a discretization of momenta of an $\hbar k$ grid with 64 points was used. The wave-function simulation was performed by simulating quantum jumps between family states with a *continuum* of quasimomenta q while representing the Bloch function on a spatial and momentum grid of 64 points. The time step Δt for integration was typically between $\Delta t=T/6$ to $T/30$ with $T=2\pi/\omega_{\rm osc}$ the classical oscillation time of the wave packet in the optical potential. Convergence of the Monte Carlo approach can be seen from a comparison of Figs. 4b) and 4(c). In practice, 10 000 realizations are sufficient to obtain a reasonably smooth spectrum. It is somewhat surprising that the semiclassical spectrum with a simple quantum correction agrees so well with the full quantum calculation. We emphasize, however, that $\frac{1}{2}$ to $\frac{3}{2}$ is a special case as the atomic coherences between the ground states are exactly zero. To calculate the spectrum, we tabulated the stationary dipole correlation function $c_{\pm1}(\tau)$ as a function of time. The time interval was chosen large enough to guarantee convergence to the asymptotic value [obtained by factorizing the correlation function in Eq. (17) for large times]. Spectra were then

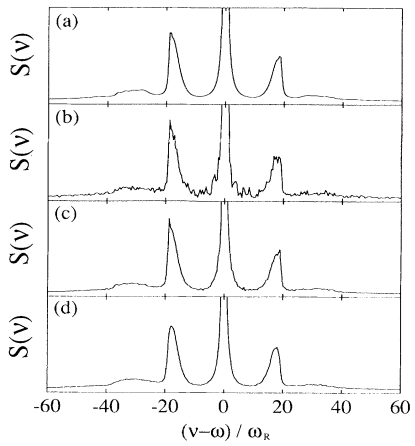

FIG. 4. Comparison of the (a) spectra of resonance fluorescence $S_{+1}(\nu)$ for a $\frac{1}{2}$ to $\frac{3}{2}$ transition obtained by discretizing the master equation (8) on an $\hbar k$ grid and computing the spectrum via the quantum regression theorem; (b) spectra from wave-function simulations (Sec. IV) with 400 realizations and (c) 80 000 realizations; (d) spectrum from a semiclassical bipotential calculation with a simple quantum correction (Sec. V). The parameters are the same as in Fig. 3. The excited states were adiabatically eliminated.

derived by taking a Fourier transform of the correlation functions.

Figure 5 shows dipole correlation functions $c_{+1}(\tau)$ for $U_0=200E_R$ (solid lines) and $20E_R$ (dashed lines). The upper portion of the figure shows the real part and the lower portion the imaginary part of $c_{+1}(\tau)$. Note that the imaginary part is much smaller than the real part. It is the small imaginary part that is responsible for the red versus blue asymmetry of the sidebands in the spectrum. The spectra for these parameters are shown in Figs. 6(a) and 6(b). The correlation functions $c_{+1}(\tau)$ in Fig. 5 show damped oscillations which for large times τ converge to a constant asymptotic value. The oscillations in $c(\tau)$ are associated with the frequencies of wave-packet oscillations in the optical potential wells $U_{\pm}(z)$ (see Fig. 2) and produce the sidebands in the spectrum. Changing the well depth gives rise to different oscillation frequencies which is reflected in different separation of the sidebands from the central frequency $\nu=\omega$ in Figs. 6(a) and 6(b). For $U_0=200E_R$ we have a deep well and fast oscillations (solid lines), while for $U_0=20E_R$ the potential well is shallow and oscillations are correspondingly slower (dashed lines). The finite asymptotic value of the correlation function leads to a coherent δ-function peak $\delta(\nu-\omega)$ in the spectrum. The decay of the correlation function as a function of time is related to the widths of the various peaks in the spectra. We will discuss this below in more detail for the sidebands and the central peak.

The central peak at $\nu=\omega$ in Figs. 4, 6(a), and 6(b) consists of the coherent δ-function peak and a superimposed incoherent spectral line of finite width. This incoherent spectrum (with the δ peak subtracted) is plotted on a larger scale in Fig. 7 for $U_0=20E_R$ (solid line), $U_0=100E_R$ (dashed line), and $U_0=200E_R$ (dash-dotted line). All three spectra are scaled to the same maximum point. From Fig. 7 we see clearly that the width of the incoherent line decreases with increasing potential well depth U_0. The inset in Fig. 7 relates this spectra line narrowing to the localization of the spatial distribution of the atoms in one of the potential wells plotted for $-\lambda/8\le z\le\lambda/8$. From this figure it is apparent that the width of the incoherent line becomes much smaller, with

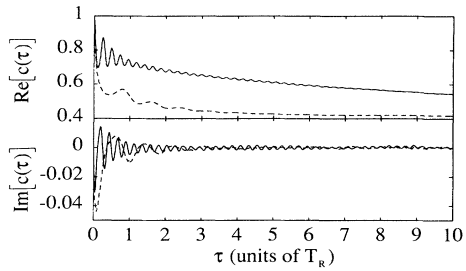

FIG. 5. Dipole correlation function $c_{\sigma=+1}(\tau)$ as a function of time τ in units of the recoil time $T_R=1/\omega_R$ for a $\frac{1}{2}$ to $\frac{3}{2}$ transition. The upper portion of the figure shows the real part, and the lower portion the imaginary part of $c(\tau)$. The solid and dashed lines correspond to $U_0=200E_R$ and $20E_R$, respectively. In both cases $\gamma_0=5/3E_R$.

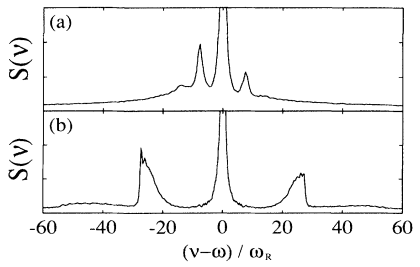

FIG. 6. Spectra of resonance fluorescence $S_{+1}(\nu)$ for the $\frac{1}{2}$ to $\frac{3}{2}$ transition of the two correlation functions shown in Fig. 5: (a) corresponds to $U_0=20E_R$ and (b) corresponds to $U_0=200E_R$. The value of γ_0 is $5/3E_R$.

increasing localization of the atoms, than the width given by optical pumping time, $\gamma_0=1.666E_R$. We identify this as a Lamb-Dicke narrowing of the line which occurs when the atomic distribution is well localized on the scale given by the wavelength of the light. The present situation is analogous to the narrowing in resonance fluorescence spectra of laser cooled trapped ions in the Lamb-Dicke limit [17].

In Appendix C we express the spectrum in terms of Raman transition matrix elements between the Bloch energy eigenstates. Let us consider these Raman matrix elements in the limit of a well-localized atomic distribution. To be specific, we assume that the atom is well localized near $z\approx 0$ in one of the lowest quantum states $|nq-\rangle$ of the $U_-(z)$ well. Assuming the spatial extent $a\ll\lambda/2$ of the states n and n', we expand the relevant Raman transition matrix elements in powers of kz corresponding to the Lamb-Dicke expansion parameter $\eta=a/\lambda\ll 1$:

$$\begin{aligned}(q,n'-|e^{-ik'\hat{z}}B_{-1}(\hat{z})|q+k'-k,n-)&=\frac{3}{\sqrt{2}}[\delta_{n'n}-i(q,n'-|k'\hat{z}|q+k'-k,n-)+\cdots]\\(q,n'-|e^{-ik'\hat{z}}B_{+1}(\hat{z})|q+k'-k,n-)&=\frac{1}{\sqrt{2}}[(q,n'-|k'\hat{z}|q+k'-k,n-)+\cdots]\end{aligned}\tag{51}$$

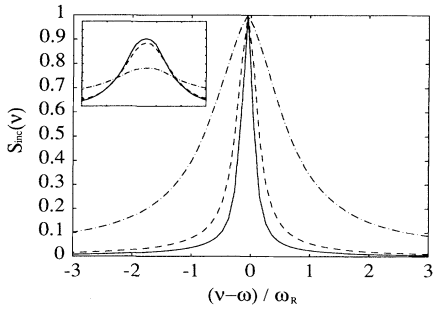

FIG. 7. The incoherent contribution $S_{\rm inc}(\nu)$ to the central line is plotted for $U_0=200E_R$ (solid), $U_0=100E_R$ (dashed), and $U_0=20E_R$ (dash-dotted) with $\gamma_0=5/3E_R$. The inset shows the corresponding spatial distributions $\langle z|R|z\rangle$ of the atoms for $-\lambda/8<z<\lambda/8$. Increasing U_0 localizes atoms in the valleys of the potential and leads to a narrowing of the spectrum.

where $(|\ |)$ denotes matrix elements obtained by integrating the Bloch functions over the unit cell $0 \le z \le \lambda/2$. The two matrix elements of $B_\pm$ in the above equation show that transitions $n \to n'$ $(n' \neq n)$ within U_- are suppressed by a factor η, while inter-well transitions $- \leftrightarrow +$, i.e., the matrix elements $(qn' - |e^{-ik'\hat{z}} B_0(\hat{z})| qn +)$, are exponentially small. The atom localized at $z=0$ experiences predominantly σ^- polarized light, so transitions $|g_-\rangle \to |e_{-3/2}\rangle$ are back are dominant; due to the small overlap between wave functions with different n, these transitions change the vibrational level only rarely. The resulting reduction of the cooling rates is reflected in a line narrowing of the spectra (Fig. 7) and slow damping time scales in the correlation functions (Fig. 5). The width of the sidebands in Figs. 4 and 6 is determined by two factors. First, due to the anharmonicity of the optical potentials the Raman transitions $n \to n \pm 1$ between the bands will have different transition frequencies (compare the vertical lines in the lower part of Fig. 3). Second, we have broadening due to optical pumping. The substructure which develops in Figs. 4 and 6 for large U_0 corresponds to the $0 \to 1$ transition and indicates that the lowest transition is almost resolved within the sidebands.

We conclude this section with a brief comparison of the computational efficiency of the direct integration of the master equation (on an $\hbar k$ grid) versus the wave-function simulation method based on propagating time-dependent Bloch functions with the split-operator FFT. In both cases the excited states were adiabatically eliminated. Within the time it takes to compute the steady-state momentum and spatial distributions for the $\frac{1}{2}$ to $\frac{3}{2}$ transitions from the master equation, approximately 115 000 realizations are done. Since typically 10 000 realizations are necessary to obtain smooth distributions, we see a clear advantage for the wave-function simulation method. For the spectrum, on the other hand, we obtain approximately 12 000 realizations within the time needed to solve the master equation and correlation function. Thus in this case we did not find a computational advantage of the simulation method. We could see the trend, however, that the Monte Carlo approach becomes more efficient for higher-order $J_g \to J_e$ transitions. All these comparisons are for a *single*-CPU computer. According to our experience, one of the central advantages of the Monte Carlo method is that it allows a trivial *parallelization* by running the same program in parallel on several computers. In practice, we have run the wave-function simulation in parallel on up to 25 medium and low-end computer workstations with a corresponding significant gain in computational speed.

VIII. CONCLUSION

We have given a theoretical analysis of resonance fluorescence from 1D molasses. We have formulated the theory for a general J_g to J_e transition. The center-of-mass motion has been treated quantum mechanically. The autocorrelation function for the atomic dipole has been calculated by numerical solution of the master equation, a wave-function simulation, and within a semiclassical bipotential model. An interpretation of the sidebands and their substructure in the spectrum has been given in terms of Raman transitions between the energy bands, and the widths and heights of these lines have been related to Raman transition rates between these energy eigenstates in the optical potential. Localization of the atomic distribution on the scale given by the wavelength (Lamb-Dicke limit) leads to a slow time scale of laser cooling which is reflected in the widths of the lines. In the present paper we have reported results for $\frac{1}{2}$ and $\frac{3}{2}$ transitions in a lin⊥lin configuration with the excited states adiabatically eliminated. We have performed similar calculations for higher angular momenta transitions and other laser configurations. These results will be reported elsewhere. It seems promising to extend the wave-function simulations using split-operator FFT methods to 2D problems [28].

ACKNOWLEDGMENTS

P. Z. thanks P. Lett, W. Phillips, S. Rolston, and C. Westbrook for discussions which initiated this work. The work at JILA is supported in part by the National Science Foundation.

APPENDIX A: EXPLICIT FORMULAS FOR THE JUMP OPERATORS

In this appendix we give the explicit formulas of different operators found in the master equation, in the adiabatically eliminated case derived in Sec. III:

$$\mathcal{D}\mathcal{D}^\dagger = \tfrac{2}{3}\{[2-\cos(2z)]|+\rangle\langle+| + [2+\cos(2z)]|-\rangle\langle-|\}\ . \tag{A1}$$

If we set $U_0 = -2/3s\Delta$, the bipotential $U_\pm(z) = (s/2)\Delta[\mathcal{D}\mathcal{D}^\dagger]_{\pm\pm}$ is

$$U_\pm(z) = \frac{U_0}{2}[-2 \pm \cos(2z)], \tag{A2}$$

$$B_0 = \frac{1}{\sqrt{2}}(\cos z\,|-\rangle\langle+| + \sin z\,|+\rangle\langle-|), \tag{A3}$$

$$B_{-1} = \frac{1}{\sqrt{2}}(3\cos z\,|-\rangle\langle-| + \cos z\,|+\rangle\langle+|), \tag{A4}$$

$$B_\pm = \frac{1}{\sqrt{2}}(\sin z\,|-\rangle\langle-| + 3\sin z\,|+\rangle\langle+|). \tag{A5}$$

APPENDIX B: PROPAGATION OF THE MULTICOMPONENT WAVE FUNCTION USING THE SPLIT-OPERATOR FFT METHOD

1. Split-operator method

According to Sec. III A the multicomponent wave function $|\phi,t\rangle \in L^2(\mathbb{R}) \otimes \mathbb{C}^N$ obeys the Schrödinger equation (18) between two spontaneous-emission events. The Hamiltonian H_{eff} has the form $H_{\text{eff}} = \hat{p}^2/2M + V(\hat{z})$. Note that $V(\hat{z}) = \sum_{i,j}^N |i\rangle V_{ij}(\hat{z})\langle j|$, with i,j atomic level indices, is an operator acting both on the center of mass and internal degrees of freedom. It is important for the

discussion below that H_{eff} can be written as the sum of two terms, the first one depending on $\hat{p}$ and the second one being a function of $\hat{z}$ alone. We define a time-evolution operator $U(t-t')=\exp[-iH_{\text{eff}}(t-t')]$. Since the exact U is not known, we approximate U for a small time step Δt by the split operator

$$U(\Delta t)=e^{-i(\hat{p}^2/2M)\Delta t}e^{-iV(\hat{z})\Delta t}+O(\Delta t^2)$$
$$\equiv U_K(\Delta t)U_V(\Delta t)+O(\Delta t)^2, \tag{B1}$$

or in symmetrized form

$$U(\Delta t)=U_K(\Delta t/2)U_V(\Delta t)U_K(\Delta t/2)+O(\Delta t^2) \tag{B2}$$

with error of order Δt^3. Details and an estimate of the error can be found in [24]. The time evolution due to $U_K(\Delta t)$ and $U_K(t)$ and $U_V(\Delta t)$ can be calculated readily in a momentum and coordinate representation, respectively,

$$U_K(\Delta t)|\phi,t\rangle=\int dp|p\rangle e^{-i(p^2/2M)\Delta t}\langle p|\phi,t\rangle,$$
$$U_V(\Delta t)|\phi,t\rangle=\int dz|z\rangle e^{-iV(z)\Delta t}\langle z|\phi,t\rangle, \tag{B3}$$

where $\langle p|\phi,t\rangle$ and $\langle z|\phi,t\rangle$ are connected by a Fourier transform. Note that U_V involves exponentiation of the N-level system matrix $V(z)$ (which has to be calculated once).

2. Discretization

We represent the wave function on a space grid in the interval $(0,L]$ by

$$|\phi\rangle=\sum_{i=1}^{n}\phi_i|z_i\rangle,\quad \phi_i=\langle z_i|\phi\rangle \tag{B4}$$

with $z_i=i\Delta z$ $(i=1,\ldots,n)$, $\Delta z=L/n$ and normalization convention

$$\mathbb{1}_{\text{c.m.}}\simeq\sum_{i=1}^{n}\Delta z|z_i\rangle\langle z_i|. \tag{B5}$$

For the momentum representation we use a grid

$$|\phi\rangle=\sum_{i=1}^{n}\varphi_i|p_i\rangle,\quad \varphi_i=\langle p_i|\phi\rangle \tag{B6}$$

with $p_i=-p_{\max}+i\Delta p$, $p_{\max}=n\pi/L$, and $\Delta p=2\pi/(n\Delta z)$. The pair ϕ_i and φ_i is connected by a discrete Fourier transformation

$$\varphi_i=\frac{1}{\sqrt{2\pi}}\sum_{j=1}^{n}e^{-iz_jp_i}\phi_j,$$
$$\phi_i=\frac{1}{\sqrt{2\pi}}\sum_{j=1}^{n}e^{+iz_ip_j}\varphi_j. \tag{B7}$$

Choosing $n=2^m$ with $m\in\mathbb{N}$, one can use the coefficient FFT algorithm which involves only $n\log_{10}(n)$ operations.

By using the FFT split-operator technique one enforces periodic boundary conditions: $\phi(z)=\phi(z+L)$. This fact makes this method well adapted for propagating the time-dependent (periodic) Bloch function introduced in Sec. IV. This Bloch function has period λ; thus choosing $\lambda=L$ we discretize the wave function in the unit cell $0\le z\le\lambda$ while the FFT guarantees the periodic continuation.

3. Band-structure calculation

We have employed the Fourier basis $(|z_i\rangle,|p_i\rangle)$ [29] to solve the band-structure eigenvalue problem (with periodic boundary conditions). The discretized Hamiltonian in this basis is

$$\langle z_i|H^{(1)}|z_j\rangle=\sum_{l=1}^{n}\{l^2\Delta p\cos[l(i-j)\Delta z\Delta p]$$
$$-2ilq\Delta p\sin[l(i-j)\Delta z\Delta p)\}$$
$$+[V(z_i)+q^2]\delta_{ij}. \tag{B8}$$

APPENDIX C: SPECTRUM AND MASTER EQUATION IN THE BASIS OF BLOCH ENERGY EIGENFUNCTIONS

The spectrum $S_\sigma(\nu)$ can be obtained by solving the set of equations (25) according to Sec. III B. In this appendix we will write out the equation for the periodic perturbed density matrix R_1 for $\frac{1}{2}$ to $\frac{3}{2}$ in the basis of Bloch eigenfunctions $|nqm\rangle$. Here n is the main quantum number, q denotes the quasimomentum, and $m=\pm\frac{1}{2}$ is an atomic state label. We derive this equation under a secular approximation valid for $\omega_{\text{osc}}\gg\gamma_0$, i.e., when the sidebands are well separated. This relates the various lines in the spectrum to Raman transitions between the energy bands. The corresponding population equations for the density matrix R can be found in Ref. [13].

Consider a matrix element of the periodic density matrix R between Bloch states $|nql\rangle,\langle nql|R|n'q'l'\rangle$. Note that by writing angular brackets, we mean integration over the interval $-\infty<z<+\infty$. The periodicity of R allows us to split up each of these integrals into a sum of integrals over the unit cell. With $z=\xi+N\lambda/2$ $(\xi\in(0,\lambda/2],N=0,\pm1,\ldots)$ we have

$$\langle nql|R|n'q'l'\rangle=\frac{1}{2\pi}\sum_{M}e^{-iM\lambda(q-q')/2}\sum_{M'}e^{iM'\lambda q/2}\int_0^{\lambda/2}d\xi\int_0^{\lambda/2}d\xi' u^*_{nq}(\xi)u_{n'q'}(\xi')e^{-iq\xi}e^{+iq'\xi'}\langle l|R(\xi,\xi'+M'\lambda/2|l'\rangle \tag{C1}$$
$$\equiv\delta\left[\frac{\pi}{k}(q-q')\right]R^{qq'}_{nl,n'l'}. \tag{C2}$$

Thus the consequence of the periodicity of R is that we can factor out the δ function in $q-q'$. In a similar way we can reduce transition matrix elements of the operators $B_\sigma(\hat{z})e^{-iu\hat{z}}$ with $u\in[-k,+k]$

$$\langle n,q,l|B_\sigma(\hat{z})e^{-iu\hat{z}}|n',q',l'\rangle=\delta\left[\frac{\pi}{k}(q-q'+u-k)\right](n,q,l|B_\sigma(\hat{z})e^{-iu\hat{z}}|n',q',l'), \tag{C3}$$

where we have used the periodicity property $B_\sigma(z+N\lambda/2)=(-1)^N B_\sigma(\hat{z})$ and introduced $(|\,|)$ as a shorthand notation for the integral of the Bloch function over the unit cell, $\int_0^{\lambda/2}d\xi\cdots$.

The correlation function $c_\sigma(\tau)$, which determines the spectrum, is given by

$$c_\sigma(\tau)=\int dq\sum_{n,l}\sum_{n',l'}(nql|B_\sigma(\hat{z})e^{-ik\hat{z}}|n'ql')R^{q}_{l;n'l',nl}, \tag{C4}$$

where $\langle nql|R_1|n'q'l'\rangle=\delta[(\pi/k)(q-q')]R^{q}_{l;n'l',nl}$.

In the secular approximation the equation for $R^{q}_{l;n+ml',nl}$ separates into blocks for $m=0,\pm1,\ldots$, which gives the spectrum for the central line, the first sidebands, etc. These equations are

$$\begin{aligned}0=&\left\{-i(\nu-E_{qn}-E_{qn+m})-\frac{\gamma_0}{2}\sum_\sigma[(n+mql|B^\dagger_\sigma B_\sigma|n+mql)+(nql|B^\dagger_\sigma B_\sigma+nql)]\right\}R^{q}_{l;n+mlnl}\\&+\frac{\gamma_0}{2}\sum_\sigma\int du\,N_\sigma(u)\sum_{l'}\sum_{n'}(n+mql|B_\sigma e^{-iu\hat{z}}|n'+mq+u-kl')R^{q+u-k}_{l;n'+ml'n'l'}(n'q+u-kl'|B^\dagger_\sigma e^{+iu\hat{z}}|nql)\\&+(n+mql|e^{-ik\hat{z}}B_\sigma|nql)R^{q}_{nlnl}.\end{aligned} \tag{C5}$$

The first term on the right-hand side of this equation contains the detuning of the emission frequency ν from the transition $n\leftrightarrow n'$ and the sum of the decay width due to Raman transitions out of the initial and final states. The second term comes from the recycling term in the master equation, while the inhomogeneous term involves the populations which weight the different lines.

[1] P. Verkerk, B. Lounis, C. Salomon, C. Cohen-Tannoudji, J. Y. Courtois, G. Grynberg, Phys. Rev. Lett. **68**, 3861 (1992).

[2] P. S. Jessen, C. Gerz, P. D. Lett, W. D. Phillips, S. L. Ralston, R. J. C. Spreeuw, and C. I. Westbrook, Phys. Rev. Lett. **69**, 49 (1992).

[3] J. W. R. Tabosa, G. Chen, Z. Hu, R. B. Lee, and H. J. Kimble, Phys. Rev. Lett. **66**, 3245 (1991).

[4] D. Grison, B. Lounis, C. Salomon, J. Y. Courtois, and G. Grynberg, Europhys. Lett. **15**, 149 (1991).

[5] C. I. Westbrook, R. N. Watts, C. E. Tanner, S. L. Ralston, W. D. Phillips, and P. D. Lett, Phys. Rev. Lett. **65**, 33 (1990).

[6] H. Meltcalf (private communication).

[7] C. Cohen-Tannoudji and W. D. Phillips, Phys. Today **43**, 33 (1990); see contributions in *Proceedings LIKE Workshop,* edited by L. Moi (ETS Editrice, Pisa, 1991); and special issues on laser cooling, J. Opt. Soc. Am. B. **6**, (1989); **2**, (1985).

[8] R. Dum, P. Zoller, and H. Ritsch, Phys. Rev. A **45**, 4879 (1992); C. W. Gardiner, A. S. Parkins, and P. Zoller, *ibid.* **46**, 4363 (1992); R. Dum, A. S. Parkins, P. Zoller, and C. W. Gardiner, *ibid.* **46**, 4382 (1992).

[9] J. Dalibard, Y. Castin, and K. Mølmer, Phys. Rev. Lett. **68**, 580 (1992); K. Mølmer, Y. Castin, and J. Dalibard (unpublished).

[10] H. J. Carmichael (unpublished).

[11] N. Gisin and I. C. Percival (unpublished).

[12] J. Dalibard and C. Cohen-Tannoudji, J. Opt. Soc. Am. B **6**, 2023 (1989); **2**, 1707 (1985).

[13] Y. Castin and J. Dalibard, Europhys. Lett. **14**, 761 (1991).

[14] Y. Castin, J. Dalibard, and C. Cohen-Tannoudji, in *Proceedings LIKE Workshop* (Ref. [7]), p. 5.

[15] Y. Castin, thèse de l'Université Paris VI, 1992.

[16] We emphasize that the sidebands in Fig. 3 are *not* the sidebands of the familiar Mollow triplet: for the present parameters these Mollow sidebands would appear much further away from the central frequency.

[17] M. Lindberg, Phys. Rev. A **34**, 3178 (1986).

[18] A. P. Kazantzev, I. Surdutovich, and V. P. Yalovlev, *Mechanical Action of Light on Atoms* (World Scientific, Singapore, 1990).

[19] G. Nienhuis, P. van der Straten, and S. Q. Shang, Phys. Rev. A **44**, 462 (1991).

[20] J. Javanainen, Phys. Rev. A **44**, 5857 (1991).

[21] P. R. Berman, Phys. Rev. A **43**, 1470 (1991).

[22] V. Finkelstein, P. R. Berman, and J. Guo, Phys. Rev. A **45**, 1829 (1992).

[23] M. Wilkens, E. Schumacher, and P. Meystre, Phys. Rev. A **44**, 3130 (1991).

[24] R. Kosloff, J. Phys. Chem. **92**, 2087 (1988).

[25] K. J. Schaefer and K. C. Kulander, Phys. Rev. A **42**, 5794 (1990).

[26] H. Risken, *The Fokker Planck Equation* (Springer, Berlin, 1984).

[27] C. W. Gardiner, *Handbook of Stochastic Methods* (Springer-Verlag, Berlin, 1985).

[28] K. Mølmer, Phys. Rev. A **44**, 5820 (1991); F. Mauri and E. Arimondo, Europhys. Lett. **16**, 717 (1991).